Citation: Li, T., Yu, S., Sun, B., Li, Y., Wang, X., Pan, Y., Song, C., Ren, Y., Zhang, Z., Grattan, K. T. V., et al (2023). Bioinspired claw-engaged and biolubricated swimming microrobots creating active retention in blood vessels. Science Advances, 9(18), eadg4501. doi: 10.1126/sciadv.adg4501

APPLIED SCIENCES AND ENGINEERING

Bioinspired claw-engaged and biolubricated swimming microrobots creating active retention in blood vessels

Tianlong Li[1]†, Shimin Yu[1,2]†, Bei Sun[3,4]†, Yilong Li[3,4]†, Xinlong Wang[3,4], Yunlu Pan[1], Chunlei Song[1], Yukun Ren[1], Zhanxiang Zhang[1], Kenneth T. V. Grattan[1,5], Zhiguang Wu[1,6,7]*, Jie Zhao[1]*

Swimming microrobots guided in the circulation system offer considerable promise in precision medicine but currently suffer from problems such as limited adhesion to blood vessels, intensive blood flow, and immune system clearance—all reducing the targeted interaction. A swimming microrobot design with clawed geometry, a red blood cell (RBC) membrane–camouflaged surface, and magnetically actuated retention is discussed, allowing better navigation and inspired by the tardigrade's mechanical claw engagement, coupled to an RBC membrane coating, to minimize blood flow impact. Using clinical intravascular optical coherence tomography in vivo, the microrobots' activity and dynamics in a rabbit jugular vein was monitored, illustrating very effective magnetic propulsion, even against a flow of ~2.1 cm/s, comparable with rabbit blood flow characteristics. The equivalent friction coefficient with magnetically actuated retention is elevated ~24-fold, compared to magnetic microspheres, achieving active retention at 3.2 cm/s, for >36 hours, showing considerable promise across biomedical applications.

INTRODUCTION

An innovative approach to deliver therapeutic agents to hard-to-reach tissues, using swimming microrobots, promises to revolutionize conventional medical practice (*1*–*7*) and is an emerging research interest in precision medicine. Conventional drug delivery strategies primarily rely on the diffusion of therapeutic molecules and micro/nanocarriers in the blood flow or in other biofluids. Although various drugs using oral or intravascular administration are available, they still suffer from clearance and a rapid transit period in the circulation system and various organs, making them both less effective and showing several side effects (*8*–*11*). Learning from natural motile microorganisms, various propulsion strategies for cutting-edge swimming microrobots have been developed for low Reynolds number environments, using magnetic and acoustic actuation to offer better delivery of therapeutic agents to the diseased region (*12*–*20*). Magnetically powered swimming microrobots have, in particular, exhibited efficient and controllable propulsion in various complex biological media such as the gastrointestinal tract, the ocular vitreous medium, and the extracellular matrix (*21*–*27*). Recent efforts have focused on locomotion in the circulatory system to offer an ideal pathway to target disease locations (*28*).

As a result, various types of magnetic swimming microrobots have demonstrated spatiotemporal navigation in the blood, ranging from the rolling motion of spherical swimmers in model blood vessels to rotational movement of helical propellers in the bloodstream (*25*, *29*–*32*). However, these approaches, while promising better locomotion in model circulation systems, suffer from inherent limitations restricting their applicability. First, typical magnetic swimming microrobots are of rigid geometry with poor biocompatibility, creating a limited circulation period in the body (*33*–*35*) and intensive rates of blood flow result in a major navigation bottleneck. Assuming a flow rate (FR) in a major vein of ~2 × 10^4 μm/s (roughly equal to travelling ~1000 body length per second for a microrobot of size ~20 μm), this results in marked challenges for them to overcome (*36*–*39*). The swimming microrobots must be retained when they arrive at the targeted site, even with intensive blood flow, to deliver the drug. Although a large number of site-specific molecule interaction-based strategies have been developed to achieve targeted retention of the drug, there is still a limitation from low precision, size constraints, and the complex surface chemistry arising from the impact of macroscale blood flow. Therefore, the challenge is to develop better magnetically powered swimming microrobots that can work well in strong blood flows and, in particular, allow active retention in blood vessels in the long term (*40*).

Natural aquatic microorganisms have evolved the capability of locomotion and retention for survival in various environments (*41*), in contrast to artificial swimming microrobots. For example, limnoterrestrial tardigrades (e.g., *Hypsibius exemplaris*) have developed motility strategies involving a claw-ground engagement mechanism (*42*, *43*), allowing them to adapt to dynamic and complex environments. Under intensive flow, their claws mechanically engage with the surrounding ground, allowing them to grip soft and rough plant matter. This strategy, although appearing inefficient on stiff matter, shows considerable performance for locomotion and retention in heterogeneous and fluid environments, thereby offering a design pathway for swimming microrobots, which can show high levels of retention in the bloodstream. However, red blood cells (RBCs) are known as natural long-circulation delivery vehicles, harnessing attractive biological features, which can be integrated into robotic system designs, and such an RBC-mimicking micro/nanoscale architecture has recently led to

---

[1]State Key Laboratory of Robotics and System, Harbin Institute of Technology, Harbin 150001, China. [2]College of Engineering, Ocean University of China, Qingdao 266100, China. [3]Department of Pancreatic and Biliary Surgery, The First Affiliated Hospital of Harbin Medical University, Harbin, China. [4]Key Laboratory of Hepatosplenic Surgery (Ministry of Education), the First Affiliated Hospital of Harbin Medical University, Harbin 150001, China. [5]School of Science and Technology, University of London, London EC1V 0HB, UK. [6]Key Laboratory of Microsystems and Microstructures Manufacturing (Ministry of Education), Harbin Institute of Technology, Harbin 150001, China. [7]School of Medicine and Health, Harbin Institute of Technology, Harbin 150001, China.
*Corresponding author. Email: zhiguangwu@hit.edu.cn (Z.W.); jzhao@hit.edu.cn (J. Z.)
†These authors contributed equally to this work.

the development of functionalizing swimming microrobots with natural RBC membranes (*44*, *45*). Such microrobots have shown unprecedented capability, such as in evading the immune system, allowing prolonged circulation in the bloodstream. It has recently been reported that the lipids in the RBC membranes could reduce friction, by using their highly hydrated phosphocholine headgroups, through using the hydration lubrication mechanism (*46*). As a result, it is proposed that a design of claw engagement, allowing reduced flow resistance and integrating the RBC membranes to swimming microrobots in blood vessels, will allow long-term retention and navigation for in vivo use.

To test the above idea, claw-engaged and RBC membrane–coated swimming microrobots have been developed in this work, showing excellent performance in magnetically actuated navigation and active retention in blood vessels in vivo (Fig. 1A and movie S1). The swimming microrobots were fabricated using clawed template-assisted controllable assembly of polymers, magnetic nanoparticles, drugs, and an RBC membrane. Combining real-time intravascular optical coherence tomography (IVOCT)–based microangiography and wireless actuation of an external rotating magnetic field (RMF), the swimming microrobots could not only perform controllable locomotion (Fig. 1B) but also showed long-term retention in the jugular vein in rabbits following magnetic actuation (Fig. 1C). The success of this work offers advances in the active targeted retention of such microrobots, achieved through investigating and optimizing the manipulation procedures, including intravascular injection through a catheter (using IVOCT), as well as microangiography-guided navigation in blood vessels, and showing extended retention when using mechanical claw engagement demonstrated in vivo. All this creates considerable promise for use in a wide range of future therapies.

RESULTS

Design and fabrication of swimming microrobots

The innovative claw-engaged and biolubricated swimming microrobots (CBSMRs) designed in this work have been based on exploiting three key criteria: (i) the enhancement of the adhesion between the swimming microrobots and the blood vessel to overcome issues with blood flow, (ii) the reduction of the resistance between the swimming microrobots and the blood flow to enhance the movement and performance and thus prevent the generation of

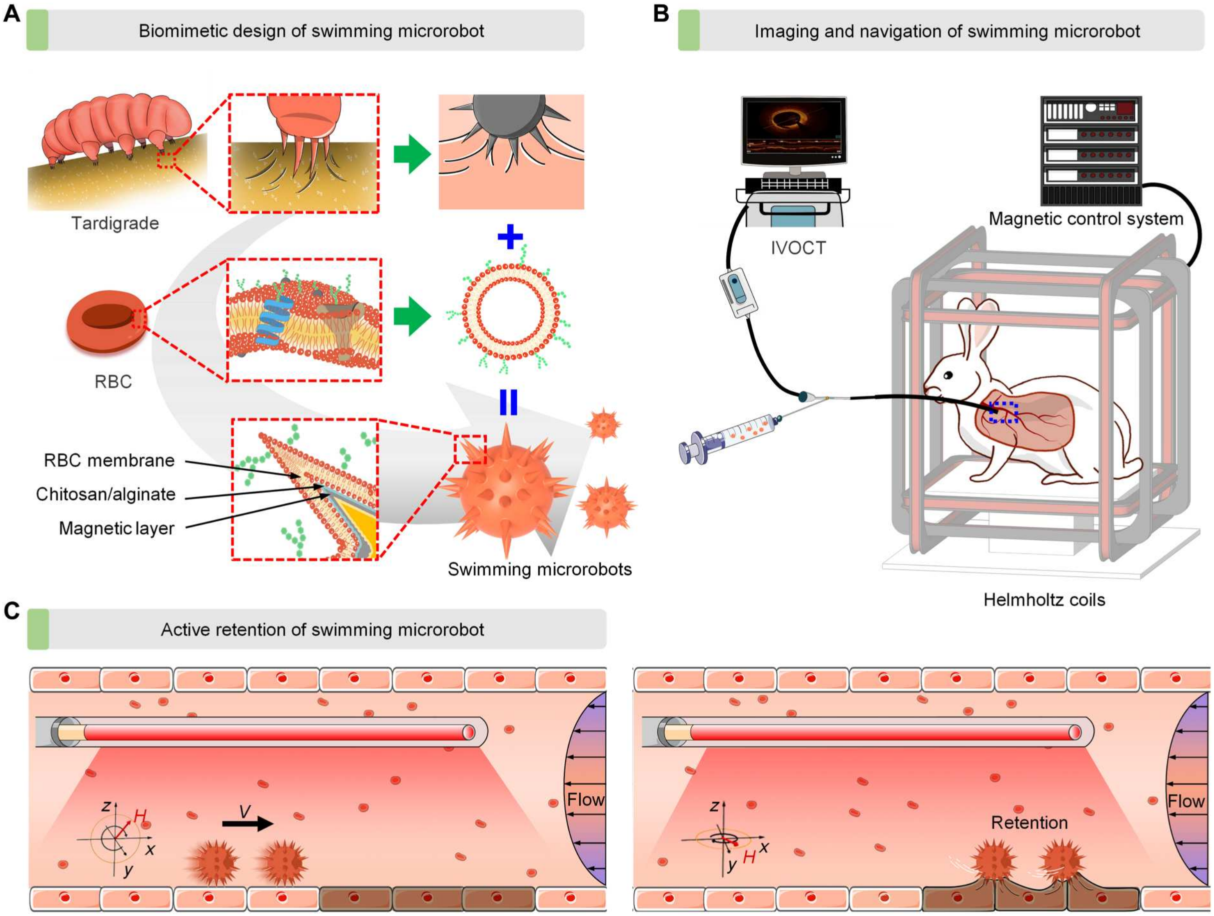

Fig. 1. Schematic overview of active navigated retention using swimming microrobots in vivo. (**A**) Conceptional development of claw-engaged and biolubricated swimming microrobots (CBSMRs). The tardigrades inspired the clawed geometry design and magnetically actuated claw engagement of the swimming microrobot, and the red blood cell (RBC) membrane–camouflaged coating was functionalized on the swimming microrobots to reduce the impact of the blood flow. (**B**) Schematic of imaging and navigation of the swimming microrobots in blood vessels of a rabbit in vivo. IVOCT, intravascular optical coherence tomography. (**C**) Navigated locomotion and active retention of the swimming microrobots in blood vessels through the manipulation of external magnetic field.

thrombus, and (iii) exploiting magnetic actuation to enhance retention on the blood vessels. Building on these important principles, a design of magnetic swimming microrobots with clawed geometry and RBC membrane coating based on a controlled assembly technique was constructed. These were evaluated using mechanical actuation in blood vessels using an external magnetic field (with uniform intensity) to accomplish the desired navigation and retention under intensive blood flow. To this end, the magnetic clawed microparticles were first prepared through the synthesis of Fe_3O_4 layers on sunflower pollen as clawed particles and the subsequent carbonization of the clawed particles (Fig. 2A) [as described in a previous report (*47*)]. Note that the size of the clawed particles can be precisely controlled within the range of 30 ± 0.8 to 8 ± 1.1 μm through thermal treatment manipulation, which was measured from the scanning electron microscopy (SEM) images in fig. S1. Although the carbonization of internal material reduced the size of the swimming microrobot, the claw shape remained intact, thereby enabling upstream movement on the surface of blood vessels. Moreover, the zeta potential of swimming microrobot was stable in the range of −10.1 to −10.8 mV over a span of 72 hours (fig. S2), which was measured by Zetasizer Nano ZS (*48*). Following that, five bilayers of chitosan (CHI)/alginate (ALG) as building blocks and the RBC membrane–derived nanovesicles (of size ~100 nm) were then fused onto the magnetic clawed particles. The high-temperature carbonization converted the biomass in the pollen into degradable carbon-based substances, and the Fe_3O_4 layers, gel layers (CHI/ALG), and RBC membrane coated in the subsequent preparation process of swimming microrobot were all degradable in body.

It has been reported previously that such RBC membrane nanovesicles have high surface tension and thus are liable to fuse onto the surface of swimming microrobots to minimize the free energy of the system (*48*). Moreover, the coating of the $(CHI/ALG)_5$ bilayers creates swimming microrobots with negative charges, ensuring the fusion of the RBC membranes nanovesicles onto the swimming microrobots with a right-side-out orientation (*49*). The SEM image shown in Fig. 2B displays the clawed geometry of the swimming microrobots. To confirm that the RBC membrane has fully coated the swimming microrobots, rhodamine B–stained RBC membrane nanovesicles were fused onto them. The fluorescent microscope image (in Fig. 2C) illustrates that the desired full coverage of the RBC membrane has been achieved. Fluorescence observations for up to 48 hours showed that the RBC membranes wrapped around the surface of swimming microrobot were stable (fig. S3). Furthermore, the Western blot analysis was used to examine the protein contents of swimming microrobots. The RBC membrane–wrapped swimming microrobots were dialyzed with 30-nm porous membranes for 24 hours to remove unbound proteins and subsequently treated with lysis buffer to solubilize the membrane proteins. Samples of RBC membrane and clawed particle were prepared in parallel as a comparison. The CD47 was selected to validate the reliability of the protein properties. As shown in fig. S4, protein separation indicates that the membrane proteins were retained throughout the fabrication of swimming microrobot and can be identified on the RBC membrane–coated swimming microrobot. This finding suggests that the RBC membrane–derived vesicles were successfully wrapped on the swimming microrobot and could improve its biocompatibility. The magnetization of the swimming microrobots was estimated using a superconducting quantum interference device and as shown in the magnetization curve (Fig. 2D), the swimming microrobots exhibited typical superparamagnetic behavior with a remanence of 8.68 electromagnetic unit (emu) g^{-1} and coercivity of 0.19 kOe, respectively.

The key desired functionalities of the swimming microrobots, which include controllable locomotion and extended retention, rely on their interaction with both the blood vessels and blood flow. Subsequently, the adhesion of the swimming microrobots to the blood vessels was evaluated using quantitative dynamic atomic force microscopy (AFM). To do so, the swimming microrobots were first immobilized on the tip of the AFM (fig. S5) and moved down toward the murine major vein vessel, and once they contact the surface of the vessel, the cantilever was moved back to its original position. For the adhesion force test, we used a rectangular silicon nitride probe that measured 450 μm in length and 50 μm in width. The approach rate and retreat rate of the probe were both set to 19.8 μm/s, and a total of 1024 data sampling points were recorded during the experiment. These experimental conditions were selected to ensure accurate and reliable measurement of the adhesion forces between the swimming microrobot and the blood vessel.

The adhesion force between the swimming microrobot and the blood vessel can be calculated through the deflection of the cantilever and knowing its spring constant, using the following equation

$$F = V \cdot \gamma_D \cdot k_N \tag{1}$$

where V, γ_D, and k_N are the deflection signal, the deflection sensitivity, and the elasticity coefficient, respectively. As shown in Fig. 2E, the adhesion force between the magnetic sphere (MS) and the blood vessels is 1.56×10^{-7} N. In contrast, swimming microrobots without such an RBC membrane coating exhibited an adhesion force with the blood vessels of 3.98×10^{-7} N. This more than twofold increase in the adhesion force demonstrates that the clawed geometry can efficiently elevate the adhesion of the swimming microrobots with the blood vessels. The adhesion force of the swimming microrobots was measured to be 2.91×10^{-7} N, a figure that is lower than that without the RBC membrane coating, confirming that this coating can reduce the adhesion of the swimming microrobots with the blood vessel. Note that the adhesion force is not equal to the friction between the swimming microrobots and the blood vessel, but it reflects the changes in the friction.

Next, the impact of the blood flow on the adhesion between the swimming microrobots and the blood vessels was studied through the measurement of the maximum FR that the swimming microrobots can overcome (Fig. 2F). The flow resistance to the swimming microrobots was calculated from the maximum FRs, using the Stokes equation, which is given below

$$F_R = 6\pi\eta R v \tag{2}$$

where η, R, and v are the dynamic viscosity of the fluid, the radius of the swimming microrobots, and the relative velocity of the swimming microrobots and flow, respectively. The value of the blood flow velocity in force calculation was used the actual velocity according the position of microrobot in the blood vessel and distribution of Poiseuille flow field.

As shown in Fig. 2F, MSs of similar size to the swimming microrobots served as a control, and the FR of the phosphate-buffered saline (PBS) shows a value of 0.05 ± 0.01 cm/s on a glass substrate, equating to a flow resistance of 6.79 ± 1.21 pN. The FR of the MSs in

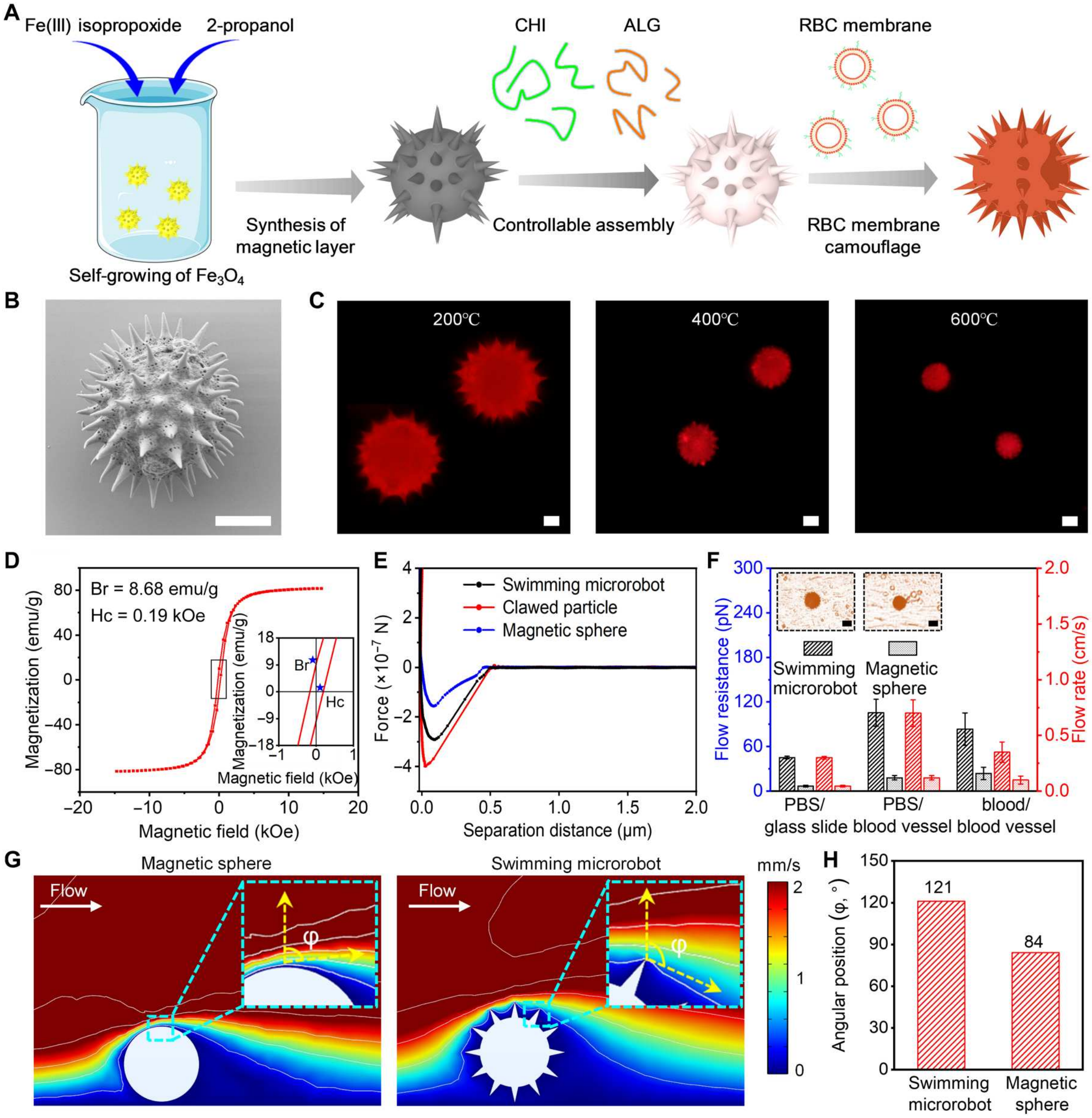

Fig. 2. Fabrication and characterization of swimming microrobots. (**A**) Schematic of the fabrication steps of the swimming microrobots. (**B**) Scanning electron microscopy (SEM) image of the swimming microrobot. Scale bar, 10 μm. CHI, chitosan; ALG, alginate. (**C**) Fluorescence microscopic images of the swimming microrobots of different sizes through manipulation of the thermal treatment (where the RBC membrane was stained with rhodamine B). Scale bars, 5 μm. (**D**) Magnetization loop from the superconducting quantum interference device analysis of the swimming microrobots. Br, remanence; Hc, coercivity; emu, electromagnetic unit. (**E**) Adhesion force analysis of the swimming microrobots using atomic force microscopy (AFM). Magnetic clawed particles and magnetic spheres (MSs) were also measured as controls. (**F**) The maximum flow resistance that the swimming microrobots can offer, using a glass slide and blood vessel as substrates and PBS and blood as flow media, respectively (the inset shows the optical image of the swimming microrobots and the MSs of the same size on the blood vessel surface). Scale bar, 20 μm. PBS, phosphate-buffered saline. (**G**) Computational simulated flow profile of the swimming microrobot and the MSs (same size as the microrobot) under flow conditions [the yellow arrows indicate the angular positions (value of ϕ) of the flow separations]. (**H**) The angular positions of the swimming microrobot and MS in the flow stream.

the blood vessels was gently elevated to 0.12 ± 0.02 cm/s with the PBS flow, which may be attributed to the enhanced adhesion from the blood vessel. The MSs in the blood vessel (under the blood flow) display a value of FR of 0.10 ± 0.04 cm/s, which may result from protein fouling effects, when subjected to the flow of blood. Note that the magnetic particles (of size 5 μm) were also used as a control, displaying an FR of <0.05 cm/s in all the treatments used (fig. S6). By comparison, the FR of the swimming microrobots in the blood vessels was highly elevated (by ~3.5 times), achieving a flow resistance of 83.60 ± 21.78 pN under blood flow. In addition, the clawed geometry can also reduce the impact of the fluid on the swimming microrobots, which may involve a similar drag reduction mechanism to that on golf balls, when compared with a smooth sphere (*50*). The simulated computational profile of the flow over the swimming microrobot is shown in Fig. 2G. Compared with the spherical particle, the flow over the swimming microrobots displays a delayed flow separation, which reduces the flow resistance from the surface pressure distribution of the swimming microrobots. More specifically, the angular position (ϕ) (which is defined as the angle between the tangent direction of the streamline at the separation point and the vertical direction) was introduced to quantify the flow separation. As shown in Fig. 2H, the angular position of the swimming microrobot (~121°) is higher than that of the smooth microsphere (~84°), suggesting that the clawed geometry could reduce the impact from the flow. Together, both the clawed geometry (which could enhance the adhesion between the swimming microrobots and the blood vessels) and the coating of the RBC membrane reduce the impact of the blood flow. These effects offer notable benefits in the propulsion of the swimming microrobots in blood vessels, compared with what is seen for MSs.

Locomotion and retention of magnetically actuated swimming microrobots on blood vessels ex vivo

The magnetically actuated propulsion of the swimming microrobots was driven by using a RMF of uniform intensity, provided by a magnetic actuation system consisting of a charge-coupled device (CCD) camera, three orthogonal Helmholtz coil pairs, and a motion planner with a closed-loop feedback modulation (fig. S7). The magnetic movement of swimming microrobots was initially investigated on smooth glass slides; microscopic image in fig. S8A illustrated the locomotion of swimming microrobots driven by the magnetic actuation system in PBS and blood without flow. The dependence of velocity of swimming microrobots on magnetic field displayed the increase as the frequency of magnetic field and then declined with frequency once reaching the step-out frequency. In this case, the swimming microrobots accomplished the maximum velocity of 389.1 ± 19.7 μm/s with a magnetic intensity of 30 mT and a frequency of 35 Hz. In control experiments, the MSs with diameter of 5 and 20 μm exhibited the similar movement behavior. As shown in fig. S8B, the average velocity of the swimming microrobots in PBS increases from 75.2 (at 5 Hz) to 288.2 μm/s (at 25 Hz), with a magnetic field of 10 mT. However, both the swimming microrobots and the MSs on the glass slide, under an optimized RMF, were easily floated under flow conditions, with FRs of >0.35 ± 0.09 and 0.05 ± 0.01 cm/s, respectively. The velocity of the swimming microrobots driven by the RMF in blood exhibited a similar tendency (fig. S8C). The above data indicate that the clawed geometry of swimming microrobots creates a minor impact on the way they move on a smooth substrate, which is similar to what is seen with natural tardigrades. In addition, the pitch angle of the driving magnetic field could affect the motion performance of the microrobots. As shown in fig. S9, the velocity of microrobots decreased with reducing pitch angle of magnetic field.

For use in practical biomedical applications, the behavior in blood vessels with the application of the RMF is crucial for the mobility of the swimming microrobots achieving a rolling motion. To investigate the behavior of the motion of the swimming microrobots in blood vessels, an ex vivo model blood vessel system using microfluidics was developed by warping a murine major vein onto the inner channel of a microfluidic system, which was filled with fresh blood plasma, allowing easy observation under a microscope.

Figure 3A illustrates a schematic of the rolling locomotion of the swimming microrobot in the blood vessels, under RMF, in the *xz* and the *yz* planes. Note that once the swimming microrobots were injected, the deviations were estimated to be 0.03 cm from the injection site to the vessels (of 0.2 mm), which creates a minor impact on the navigation of the swimming microrobots on the vessels (fig. S10).

The effect of the RBC membrane coating upon the motion of the swimming microrobots on the blood vessels was examined. In static blood plasma, the swimming microrobots without the RBC membrane coating exhibited a gentle wobble behavior and remain immobile under the RMF in the *xz* plane (with a maximum field of 30 mT used). This reflects that the adhesion of the clawed structure in the blood vessels is too high to be overcome for magnetic locomotion of the swimming microrobots to occur. In contrast, a number of swimming microrobots with the RBC membrane coating showed a straight movement in the blood vessels, indicating that the RBC membrane coating was effective to modulate the adhesion of the swimming microrobots in the blood vessels (fig. S11).

To evaluate the movement of the swimming microrobots in the flow, a set of controls were used with different geometries and surface coatings. A microscope image in fig. S12 showed the magnetic motion of both MSs (sizes of 20 μm and 5 μm) under RMF with 30 mT and 30 Hz against an FR of up to 0.15 cm/s. Once the FR of the blood plasma was elevated to 2.1 cm/s (comparable to physiological blood flow in major vein), both MSs were rapidly detached from the blood vessel, followed by drift along the blood flow, reflecting the insufficient adhesion to the blood vessel. To overcome this issue, magnetic clawed particles were used. As shown in Fig. 3B, although the magnetic clawed particles allowed for the stable adhesion on the blood vessel with a FR of 2.1 cm/s, they remained stationary under the RMF (30 mT and 30 Hz, as before). In contrast, swimming microrobots under an RMF (30 mT and 30 Hz) exhibited magnetic movement under blood flow of 2.1 cm/s. The dependence of the velocities of the swimming microrobots under RMF (30 mT and 30 Hz) on the blood FR was further estimated quantitatively. As illustrated in Fig. 3C, the average velocity of the MSs (5 μm) under the RMF in the *xz* plane (30 mT) was markedly decreased from 32.8 μm/s under an FR of 0 cm/s to 4.8 μm/s under an FR of 0.15 cm/s. The MSs (20 μm) exhibited similar behavior, with slightly higher FR to overcome (0.3 cm/s). In contrast, the swimming microrobots exhibited mobility with the impact of the blood flow, their velocities being reduced from 202.8 ± 22.3 μm/s in the absence of flow to 56.0 ± 12.0 μm/s against a FR of 2.1 cm/s. Furthermore, the percentage of the swimming microrobots under the RMF in the *yz* and the *xz* planes as a function of the FR was quantified. The majority of swimming microrobots (94%) exhibited a magnetic rolling motion, with an FR of 0.3 cm/s, and 33% of the swimming microrobots achieved magnetic propulsion, with an FR of 2.1 cm/s (fig. S13), which is comparable to physiological blood flow in an abdominal vein. Figure S14 compares the upstream velocity of the swimming microrobot at different FRs in the blood, plasma, and PBS. The results indicate that the movement velocity of the swimming microrobot in the blood was similar to that in plasma, and both were lower than the velocity in PBS. This finding supports the use of plasma instead of blood in in vitro experiments.

The flow field distribution around rotated swimming microrobot and MS were also analyzed. As shown in fig. S15, the claw-engaged swimming microrobot induced a larger distribution of surrounding flow velocity than MS under a RMF at 10 Hz. In

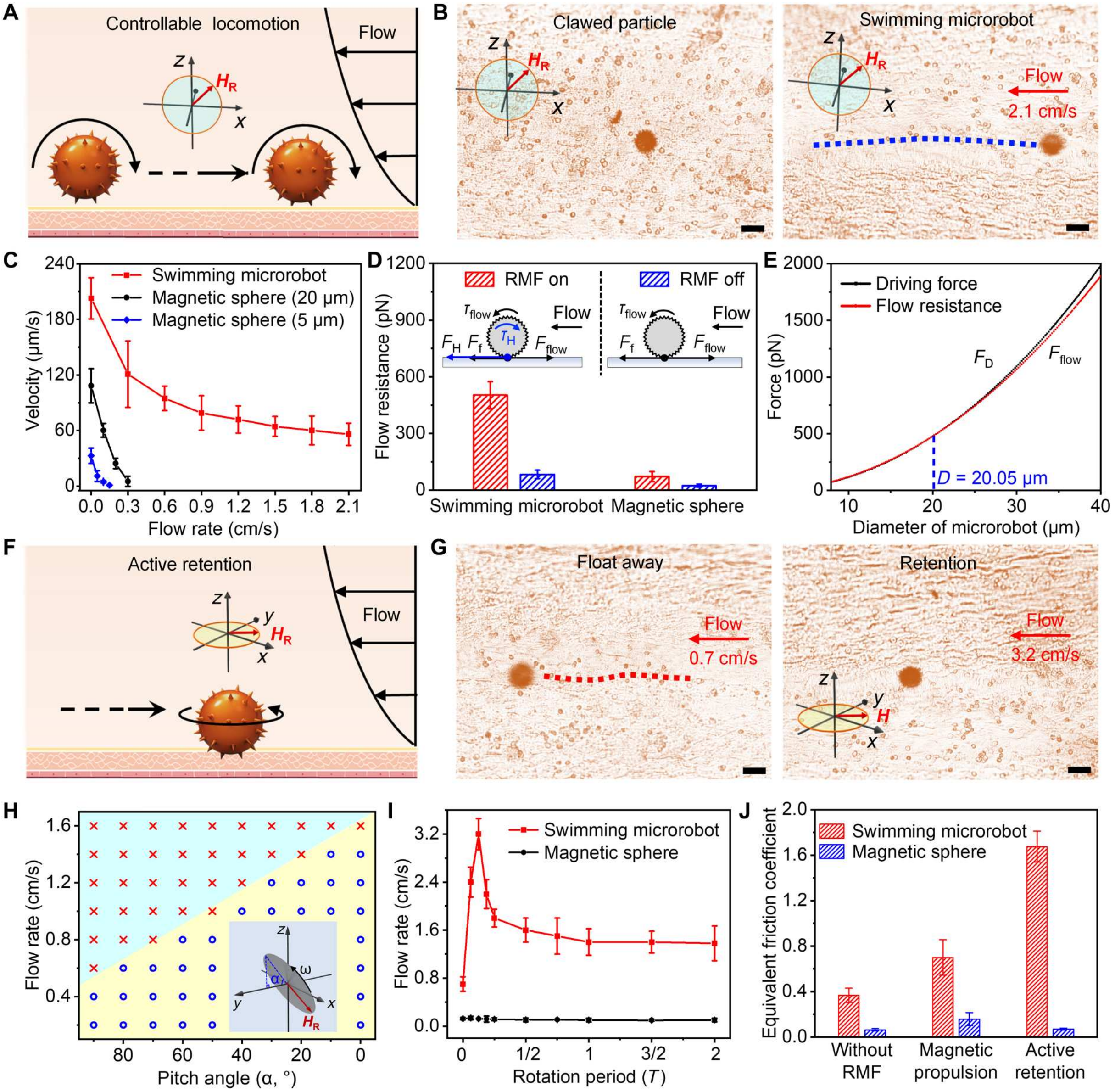

Fig. 3. Magnetically actuated locomotion and retention of swimming microrobots in blood vessels. (**A**) Schematic movement of the swimming microrobot in the blood vessels under a rotating magnetic field (RMF) in the *xz* plane. (**B**) Time-lapse images showing the magnetic motion of the magnetic clawed particles and the swimming microrobot in the blood vessel with a flow rate (FR) of 2.1 cm/s. The blue dashed line indicates the path of the microrobot's upstream motion. Scale bars, 30 μm. (**C**) Velocity of the swimming microrobots and the MSs (sizes of 20 and 5 μm, respectively) as control upon the flow at different rates. (**D**) Flow resistance of the swimming microrobot and the magnetic particles, with maximum FR. Schematic illustrating the force analysis of the swimming microrobot with the RMF on (left) and RMF off (right) (in inset). (**E**) Dependence of the magnetic actuation force and the flow resistance on the size of the swimming microrobots (with an FR of 2.1 cm/s). (**F**) Schematic of the magnetically actuated retention of the swimming microrobots in the blood vessels through the manipulation of the RMF. (**G**) Time-lapse images showing the dynamics of the swimming microrobots and the microrobots with the RMF applied in the *xy* plane in the presence of blood flow. Scale bars, 30 μm. The red dotted line indicates the motion path of the microrobot floating away with the blood flow. (**H**) The phase diagram showing the FR that swimming microrobots can overcome, in the presence of the RMF, with different rotation angles. (**I**) Retention of the swimming microrobots in the presence of the flow, under different periods of rotation, with a rotation angle of 0°. (**J**) Equivalent friction coefficient (EFC) of the swimming microrobots with different magnetic actuation conditions (MSs were used as controls).

particular, local intensive flow fields were induced between the adjacent claw structures, which reduced the flow resistance. Furthermore, a force analysis of the magnetically actuated rolling movement of the swimming microrobots within the blood vessels, in response to the flow, was carried out. As shown in the schematic illustration in Fig. 3D, the force from the local flow (F_{flow}) and the friction in the horizontal direction (F_{f}) reached a balance in the *xz* plane, under the flow of the magnetic particles, in the absence of RMF. Thus both forces are the same in value, but opposite in direction. F_{f} can be obtained through the calculation of the value of F_{flow} at the maximum rate. By comparison, when the swimming microrobots experienced magnetic actuation to achieve upstream motion, the friction in the horizontal direction and the driving force from the magnetic actuation (F_{H}) were balanced with the force from the local flow. In this case, the force from the local flow (F_{flow}) is roughly balanced with the friction in the horizontal direction (F_{f}) and the force from the magnetic actuation (F_{H}), resulting in upstream movement due to the magnetic effect, enabling the swimming microrobot to overcome the higher FR (than is seen without the magnetic actuation).

From the data on the FR shown in Fig. 3C, the value of F_{flow} for controlling the MSs (20 μm) was calculated as 23.89 pN without RMF and 71.66 pN in F_{flow} with RMF. By contrast, the values of F_{flow} for the swimming microrobots were estimated to be 83.60 pN without RMF in the *xz* plane, and 503.04 pN with RMF in the *xz* plane, respectively. The nearly sevenfold rise in the value of F_{flow} suggests that the swimming microrobots can effectively move in the blood vessels with intensive flow (Fig. 3D). Moreover, the impact of the force on the swimming microrobots of different sizes, with an FR of 2.1 cm/s, was computationally determined. As illustrated in Fig. 3E, with the size of the swimming microrobots ranging from 8 to 20.05 μm, the value of F_{flow} on the swimming microrobots was seen to be higher than that of driving force (F_{D}), implying that swimming microrobots with a size below 20.05 μm could not overcome the flow, with a rate of 2.1 cm/s. Furthermore, F_{flow} and F_{H} each reached a critical value with a size of 20.05 μm. The above analysis provides key design data for the optimum clawed geometry and robot size, with the RBC membrane coating offering the capability of swimming microrobots having upstream mobility under intensive blood flow in major vein vessels.

Maintaining the retention of the swimming microrobots in the flow stream is crucial, after their arrival at the predetermined region. One major challenge is the disappearance of F_{H}, following the removal of RMF, leading to insufficient forces to maintain the swimming microrobots in the blood vessel. For example, once RMF in the *xz* plane was removed, the swimming microrobots immediately floated away, with a blood FR of 0.7 cm/s (Fig. 3G). To overcome this issue, an attempt was made to enhance the interaction between the swimming microrobots and the blood vessel through claw-ground engagement by manipulating RMF (Fig. 3F). As an example, the application of RMF in the *xy* plane for 1 s resulted in the retention of the swimming microrobots with a blood FR of 0.7 cm/s (Fig. 3G). Furthermore, the relationship between the retention effects of the swimming microrobots and the direction and period of RMF was investigated. The pitch angle, α, of RMF, which is defined as the angle between the magnetic field tilt relative to the *xy* plane of the magnetic field, was first used for the quantitative direction of RMF. As shown in the phase diagram in Fig. 3H, the period for the magnetic actuation was 1 s, and the red crosses indicate the swimming microrobots were lost from the blood vessels with the flow, while the blue circles indicate the successful retention of the swimming microrobots in the blood vessels. FR of the swimming microrobots under RMF (for 1 s) increases from 0.4 (with α equals to 90°) to 1.4 cm/s (with α equals to 0°), indicating that RMF in the *xy* plane offers optimal retention effects for the swimming microrobots. Furthermore, the impact of the period of RMF in the *xy* plane on the retention of the blood vessel was investigated through the measurement of FR. As shown in Fig. 3I, the swimming microrobots under RMF in the *xy* plane (for one-eighth period) reached the maximum retention effect that enabled their maintenance in the vessel, with a FR of 3.2 cm/s. It was noted that the control MSs (20 μm) flowed away (with a flow with rate above 0.15 cm/s) under the same RMF as the swimming microrobots. The above data verify that their improved retention may be mainly attributed to the adhesion of the mechanical claw of the swimming microrobot on the vessel.

To quantify the retention effects of the swimming microrobots under the flow in the blood vessel studied, the equivalent friction coefficient (EFC; μ) was defined as

$$\mu = \frac{3F_{\mathrm{flow}}}{4\pi R^3 g(\rho_{\mathrm{robot}} - \rho_{\mathrm{plasma}})} \tag{3}$$

where ρ_{robot} and ρ_{plasma} are the density of the swimming microrobot and the plasma, respectively. EFC is used to evaluate the capability of the swimming microrobots in the blood vessels with different behaviors including: without RMF, upstream motion under RMF in the *xz* plane (upstream), and retention under RMF in the *xy* plane for 1 s (retention). As shown in Fig. 3J, the control MSs display the following EFC values: 0.14 without RMF, 0.42 with magnetic motion, and 0.19 with magnetic retention with RMF in the *xy* plane. The minor change in the different treatments exhibits that the RMF play a negligible role on the retention effect of the MS structures on the blood vessels.

In contrast, the EFC of the swimmer microrobots was elevated to ~0.49, a result that may be attributed to the effect of their clawed geometry on the blood vessel. Moreover, the EFC of the swimming microrobots was further increased to 2.96, with the application of the RMF in the *xz* plane (with a frequency of 30 Hz and an intensity of 30 mT). Note that the frequency and intensity of the RMF in the *xz* plane has a minor effect on the EFC of the motile swimming microrobots. The EFC value reached 4.51 (an increase of ~24 times compared with the control situation), with the application of the RMF in the *xy* plane. Swimming microrobots can still achieve good vascular retention with a blood FR of up to 3.2 cm/s with the RMF applied in *xy* plane, and this allows them to show active retention in major veins. Looking at these effects together, the swimming microrobots were found capable of both controllable locomotion and effective active retention in blood vessels in the presence of a substantial FR, taking advantage of the enhanced adhesion from both the clawed geometry and the magnetic actuation.

Magnetic dynamics of swimming microrobots in mice in vivo

To investigate the behavior of the swimming microrobots in the presence of the RMF in vivo, an autonomous navigation system that was integrated with the magnetic field and a microscope was established to modulate the magnetic actuation of the swimming microrobots in venous vessels under blood flow conditions. As can be seen in the schematic illustration (Fig. 4A) and the actual photograph (in Fig. 4A and fig. S16), the mice were first anesthetized and then injected with anticoagulant. To observe the dynamics of the swimming microrobots in vivo with the microscope, the microfluidic-based model blood vessel system was catheterized with the intraperitoneal vein of the mice to divert blood flow into a closed loop (which then returns to intraperitoneal vein).

A microscope-coupled CCD camera was used to capture the top view of the workplace, enabling the system to extract environmental information and detect the real-time position of the microrobot through image recognition. The use of a computational path planner can generate an optimal pathway and offer high localization

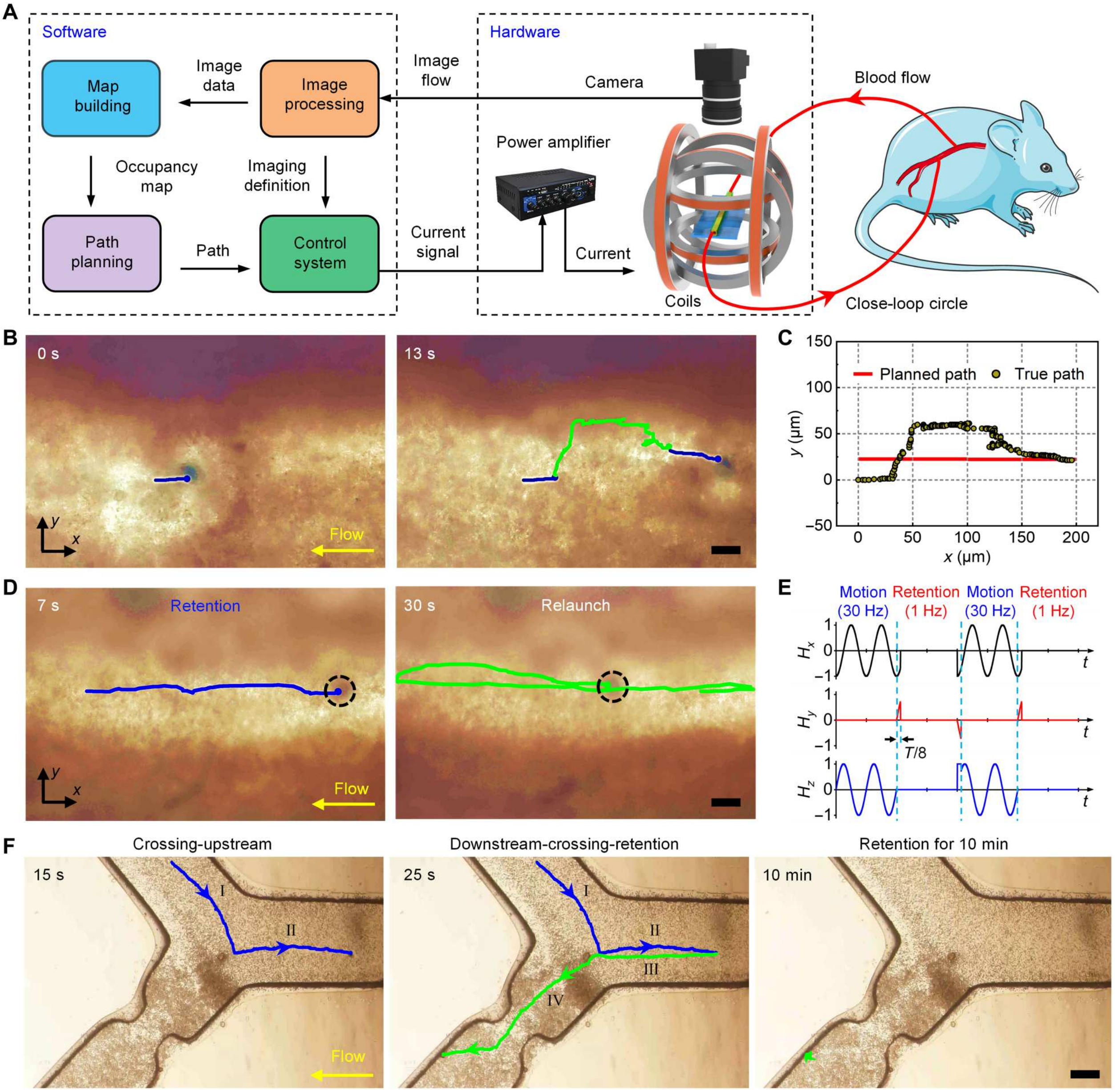

Fig. 4. Active navigated retention of swimming microrobots on the intraperitoneal vein of mice in vivo. (**A**) Schematic autonomous control of swimming microrobots on blood vessel of mice. (**B**) Time-lapse images showing the self-correcting of path deviation of swimming microrobots on blood vessel. The blue and green lines represent the trajectories of the microrobot's normal magnetic-driven motion and path self-correcting motion, respectively. Scale bars, 50 μm. (**C**) Comparison between the estimated route and actual path of autonomous navigation for the swimming microrobot in the process of path self-correcting. (**D**) Time-lapse images showing the multiple launch and retention of swimming microrobots on blood vessel. The blue line and the green lines represent the motion trajectories of microrobot in consecutive two movement-retention, respectively. Scale bars, 50 μm. (**E**) Input voltage signal of the coil group in the *x*, *y*, and *z* directions of the Helmholtz coil corresponding to twice motion-retention. (**F**) Time-lapse images illustrating the controllable locomotion and extended retention of swimming microrobots on model thrombus which was connected with mice. I-II-III-IV, crossing-upstream-downstream-crossing. Scale bar, 150 μm.

accuracy. The magnetic navigation of the swimming microrobots along the predeterminate route was undertaken using the Helmholtz coils. A computational planner of the navigation system was developed on the basis of mainly four modules: (i) the image processing module that simultaneously received and scanned images from the camera into data to monitor the position of the swimming microrobots and their predetermined destination; (ii) the map building module that generates an occupancy map using the scanning data and locates the initial position of the swimming microrobot by the similarity change curves; (iii) the path planning module that plans a feasible path according to the map the initial position, target position, and distribution characteristics of the magnetic field; and (iv) the controller module that controls the power amplifier and thus the output currents used to drive and simultaneously correct the swimming microrobot to allow it to move along the planned path.

Time-lapse images (shown in fig. S17A and movie S2) display the magnetic movement of the swimming microrobots in the blood flow in vivo. The blood FR that was introduced from the murine vein was estimated to be ~2 cm/s. Upon the application of the RMF in the *xz* plane (30 mT and 30 Hz), the swimming microrobots moved against the blood flow, with a slight deviation in direction (movie S3). The data shown in fig. S17B illustrate the deviations of the swimming microrobots in terms of their instantaneous velocities. These deviations in direction and velocity may be attributed to the impact of the RBCs in the blood flow and the changes of the tissue surface. To examine the autonomous navigation in the blood flow, a swimming microrobot was manually deviated away from estimated path, for ~25 μm and along a planned pathway. At this point, the digital data from the microscope used for the visual positioning of the swimming microrobot were input to the computational planner to identify any errors and thus simultaneously steer the microrobot. Time-lapse microscopic images (seen in Fig. 4B and movie S4) show the trajectory of the self-correction of the path of the deviated swimming microrobot. The estimated planning path and actual trajectory can be seen from Fig. 4C, where the red solid line and the black circles show the planning path and the positions of the tracked microrobot, respectively. At first, the motion trails of the swimming microrobot deviated from the planned path (with a trajectory of ~40 μm), and then the computational planner detected this problem and issued an instruction to adjust the direction of movement of the swimming microrobot to return to the planned path. Through the use of multiple feedback signals (used to correct the direction of the motion), correction of the trajectory was lastly achieved, under flow conditions, and during a 120-μm locomotion of the microrobot.

Next, we examined the active navigated retention on the vein tissues in vivo. Time-lapse images in Fig. 4D illustrate locomotion and retention of swimming microrobot in blood flow through the manipulation of RMF between *xz* plane and *xy* plane (movie S5). Upon RMF in *xz* plane (30 mT and 30 Hz), swimming microrobots locomote with velocity of 62.1 μm/s against the flow with rate of 2 cm/s. Once arrival at targeted position, RMF was swift from *xz* plane (30 mT and 30 Hz) to *xy* plane (30 mT and 1 Hz) for one-eighth period, and swimming microrobot enabled retention on the blood vessel upon blood flow. Notably, such retention behavior is reversible. Operation of reversing RMF in *xy* plane for one-eighth period and subsequent RMF in *xz* plane through inputting voltage signals of the coil group in *x*, *y*, and *z* axes, as shown in Fig. 4E, resulted in the relaunched movement of swimming microrobots upon blood flow. Relaunched microrobot was capable of actively locomoting upstream and downstream in flow blood and could be retained again at next target position.

To explore the active navigated retention of swimming microrobots under blood flow in vivo, a typical thrombosis model for targeted delivery, which has a "Y" shape and murine vein-embedded microchannel and catheterized with the intraperitoneal vein of mice in close-loop circle, was developed to mimic regions of living blood vessels with 85% lumen obstruction based on previous report (Fig. 4F and movie S6) (*51*). Upon blood flow from intraperitoneal vein of mouse, swimming microrobot initially exhibited upstream movement under RMF in *xz* plane was navigated from the upper unobstructed branch to the right arterial and then back to the lower branch through manipulation of RMF in *yz* plane. Subsequently, swimming microrobot was navigated through the obstructed microchannel via adaptive path planning. Last, the application of RMF in *xy* plane for one-eighth period endowed the retention of swimming microrobots under continuous blood flow conditions for more than 10 min. Figure S18 further illustrates the velocity of swimming microrobots during locomotion in the thrombosis model. The instantaneous velocity of the swimming microrobot fluctuated greatly, and the average velocity in different modes was substantially different. Note that the average velocity of the swimming microrobot reached 419.4 μm/s in the downstream mode, which was much higher than the velocity of 112.4 μm/s in crossing mode and the velocity of 68.6 μm/s in upstream mode. Such a navigation system was demonstrated highly promising for their autonomous operation in complex dynamic settings and unpredictable scenarios.

Active navigated retention of swimming microrobots on jugular vein of rabbits in vivo imaged with an IVOCT system

To better meet the practical application, the swimming microrobots were introduced into a clinical IVOCT system for real-time imaging and control on jugular vein of rabbits in vivo. The experimental setup for jugular vein in vivo experiments of swimming microrobots with an IVOCT imaging system is shown in fig. S19. Briefly, we used rabbits as experimental animals and catheter IVOCT into their jugular vein. The model drug, doxorubicin (DOX), was loaded into swimming microrobots for investigation of active navigated retention. To visualize the blood vessels of swimming microrobots with IVOCT, the rabbits were anesthetized, and then catheter with optical fiber of IVOCT was implanted into the jugular vein of rabbits. Subsequently, saline was ejected from catheter before imaging to repel RBCs for clear observation, otherwise the imaging of IVOCT on blood vessels became nearly detectable with the presence of RBCs within the observation range (fig. S20). To evaluate active navigated retention of swimming microrobots in vivo, equivalent amounts of MSs (MS group), MSs upon exposure to RMF (MS + RMF group), swimming microrobot (robot group), swimming microrobot upon exposure to RMF (robot + RMF group), and saline (saline group) were incorporated with saline and injected into jugular vein of rabbits through IVOCT catheter (Fig. 5A). Note that the operation of RMF was carried out with a homemade magnetic control system (fig. S19), and the magnetic actuation for propulsion of swimming microrobots was carried out for 10 min. The initial position from the observation of IVOCT was set as 0 cm (Fig. 5B). Comparing with the swimming

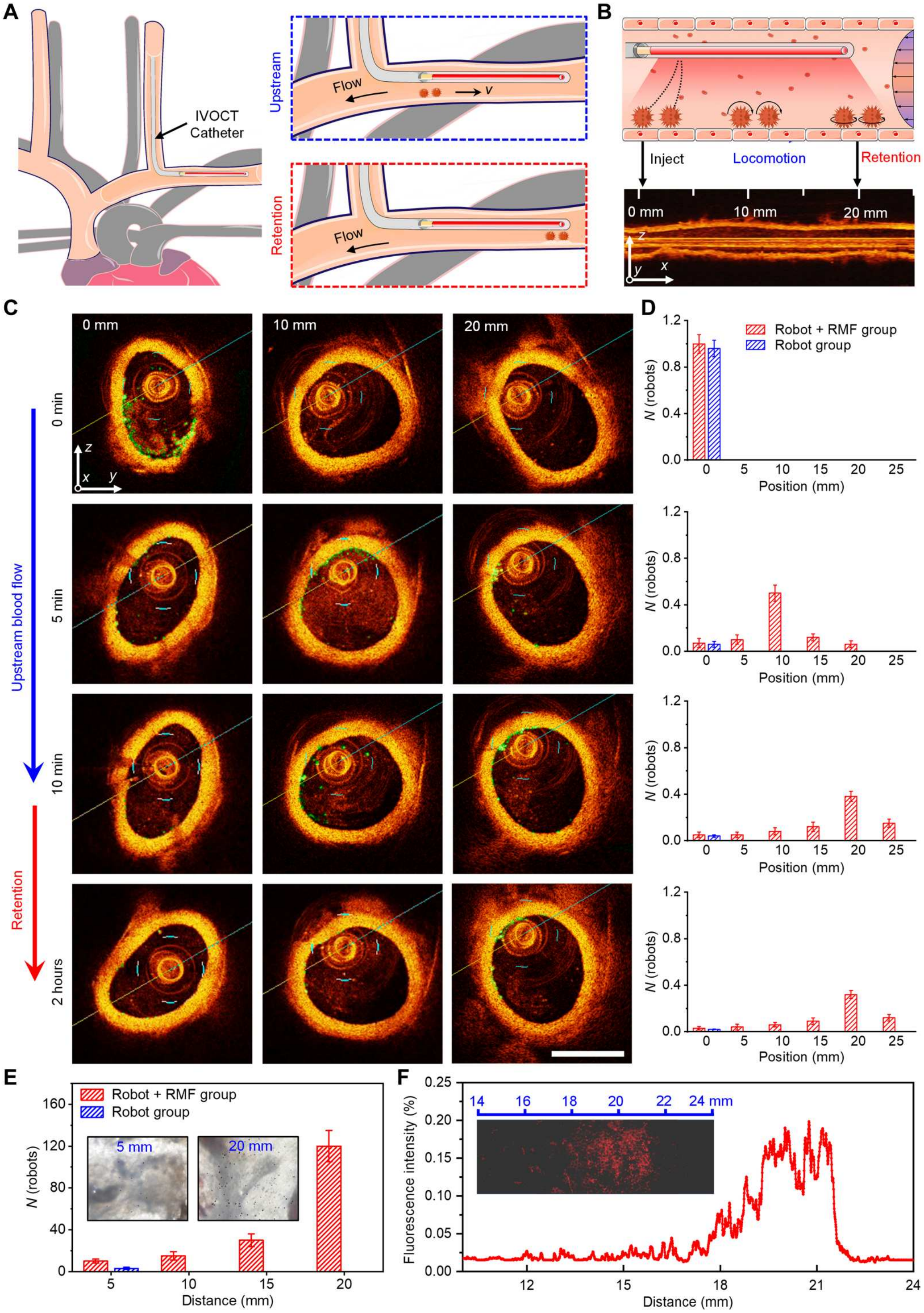

Fig. 5. IVOCT evaluation of active navigated retention of swimming microrobots on jugular vein of rabbit in vivo. (**A**) Schematic illustrating the investigation of localization and active retention of swimming microrobot on blood vessels. (**B**) Schematic and IVOCT images of initial position, locomotion, and retention of swimming microrobots in vivo. (**C**) Time-lapse IVOCT images of swimming microrobots (robot + RMF group) in different positions as function of time. RMF of 30 mT and 30 Hz was carried in *yz* plane during 0 to 10 min and changed to *xy* plane at 10 min. The green spots were indicated as signal from swimming microrobots. (**D**) Corresponding normalized number of swimming microrobots counted from green spots in (C), displaying the distribution of swimming microrobots on blood vessels upon magnetically actuated locomotion and retention. Experimental statistics were summarized from parallel experiments performed on five rabbits. Error bars represent the SDs from five independent measurements. All data are normalized to their maxima. Scale bar, 1 mm. (**E**) Microscopic images displaying active retention of the swimming microrobots and control MSs on blood vessels in vivo. Scale bar, 1 mm. (**F**) Fluorescence analysis of the distribution of swimming microrobots after active navigated retention in vivo.

microrobot, the MS injected into the jugular vein first landed at the initial position (0 mm), and then most of it were washed away by the blood flow (fig. S21). As shown in fig. S22, cross-sectional scans in saline group, MS group, and MS + RMF group display the usual profile of vessels, where negligible spots were observed at the boundary between vessel and blood, suggesting that they flowed away along the blood stream.

Moreover, time-lapse images in fig. S23 display the dynamics in robot group. A number of spots in robot group occurred at vessel-blood boundary in position of 0 cm, and these spots indicate the signal from swimming microrobots and were labeled with green color. The major swimming microrobot in robot group was periodically disappeared in 5 min. In contrast, the cross-sectional scans in robot + RMF group exhibited that nearly equal number of swimming microrobots to robot group was presented at position of 0 cm at 0 min (Fig. 5C). As magnetic actuation along blood vessels, the signal of swimming microrobot reduced at position of 0 cm and then increased in 10 min at positions of 10 and 20 mm, respectively. Once RMF for magnetic movement was turned off, the signal of swimming microrobots were quickly decreased and lastly vanished in 30 s, implying that swimming microrobots were floated away by blood flow (fig. S24).

To overcome this issue, application of RMF in *xy* plane was conducted to trigger active retention of swimming microrobots. The cross-sectional scans with IVOCT in Fig. 5C exhibited swimming microrobots remained on jugular vein for more than 2 hours (movie S7). Furthermore, the dynamic distribution of swimming microrobots on jugular vein was quantified by calculating the number of swimming microrobots on cross-sectional scans of OCT. As shown in Fig. 5D, the majority of swimming microrobots in both robot group and robot + RMF group were initially located at position of 0 cm. Ninety-four percent of swimming microrobots in robot group disappeared in 5 min. In contrast, the distribution of swimming microrobots in robot + RMF group exhibited directional change as function of time. Fifty percent of swimming microrobots were appeared at position of 10 cm upon administration for 5 min, and the position of 20 cm showed a high distribution (38%) of swimming microrobots upon administration for 10 min. The periodical change of distribution indicates the magnetically actuated navigation of swimming microrobots on blood vessels. Moreover, the distribution of swimming microrobots upon magnetically actuated retention was mainly remained after administration for 36 hours, suggesting the accomplishment of active retention on jugular vein in vivo (fig. S25). Note that such 36 hours for active retention on jugular vein of rabbits in vivo were limited by the IVOCT; the actual period would be longer than that.

Moreover, these jugular veins were collected to estimate the active retention of swimming microrobots. As illustrated in Fig. 5E, robot group exhibited only two swimming microrobots resident on jugular vein at position of 5 cm. By the contrary, 11 swimming microrobots in robot + RMF group still existed on jugular vein of rabbit at position of 5 mm, and 120 swimming microrobots were retained at position of 20 mm. In addition, the distribution of fluorescence in DOX spectrum on jugular veins was also tested to study the retention effect. Figure 5F exhibits 67% of fluorescence on the jugular vein in robot + RMF group that were located at a position between 18 and 21 mm. The above results indicate that the active navigated retention of swimming microrobots facilitates an extraordinary directionality and precision under the control of magnetic field, which is basically consistent with the observation of their locomotion and retention under the microscope. Approximately 60% of DOX was released by quantifying the DOX concentration from the extracted blood vessel using a Tecan Infinite M200 plate reader based on absorbance readings at 480 nm.

Biocompatibility and biodegradability of the swimming microrobots are important for biomedical applications. The materials of the swimming microrobots such as CHI, ALG, and iron oxides are known to be biocompatible. To measure the cytotoxicity of swimming microrobot, we tested the effect of the swimming microrobot on cell viability by a tetrazolium-8-[2-(2-methoxy-4-nitrophenyl)-3-(4-nitrophenyl)-5-(2,4-disulfophenyl)-2H-tetrazolium] monosodium salt (CCK-8) assay method. The CCK-8 assay was carried out with human umbilical vein endothelial cell line HUVEC [the American Type Culture Collection (ATCC)]. As shown in Fig. 6A, the swimming microrobot coated with RBC membrane had no effect on cell proliferation. To further evaluate the toxicity of the swimming microrobots in vivo, a comprehensive blood cell count and blood chemistry panel were conducted 24, 48, and 72 hours after administration (Fig. 6, B and C). Compared with untreated control group, the levels of all serum biochemistry markers and numbers of blood cells (RBCs, white blood cells, and platelets) receiving swimming microrobot treatment remained at normal levels. The negligible changes in metabolic biomarkers and blood cell counts indicate the minor toxicity of the swimming microrobots.

Hematoxylin and eosin (H&E) histological sections of major organs were further used to evaluate the biosafety of the swimming microrobot. We intravascularly administered PBS or the suspension of swimming microrobots to healthy rabbits once a day for two consecutive days. As shown in Fig. 6D, negligible pathological abnormalities or inflamed cells in the jugular vein, jugular artery, postcava, heart, lung, kidney, liver, or spleen in the treated model groups were observed, demonstrating the negligible toxicity of swimming microrobots toward the blood vessel and other tissues. Furthermore, the D-dimer of blood was further measured to evaluate the blood clotting disorder of the swimming microrobots in vivo. In contrast of control groups without RBC membrane, the D-dimer of blood from swimming microrobots treatment exhibited gentle change in 36 hours (fig. S26). As other controls, The RBC membrane–coated silica particles with same size as swimming microrobots displayed a nearly sixfold increase in D-dimmer after administration for 36 hours, indicating that the coating of RBC membrane prevent the formation of blood thrombus upon the treatment of swimming microrobots. Overall, these results suggested that the swimming microrobot is safe to use for drug delivery in vivo.

DISCUSSION

In this research, we have recognized three major issues that inhibit to the use of swimming microrobots for the practical delivery of therapeutic agents as follows. First are key biocompatibility and biodegradability issues, which are crucial for achieving a prolonged lifetime of swimming microrobots in the body. It is well known that conventional swimming microrobots, composed of inorganic materials or metals, face immune attack following their entry into the blood stream. Second, locomotion in main blood vessels, such as the jugular vein (in which the blood FR reaches the centimeter per second scale), is required to be demonstrated for the swimming

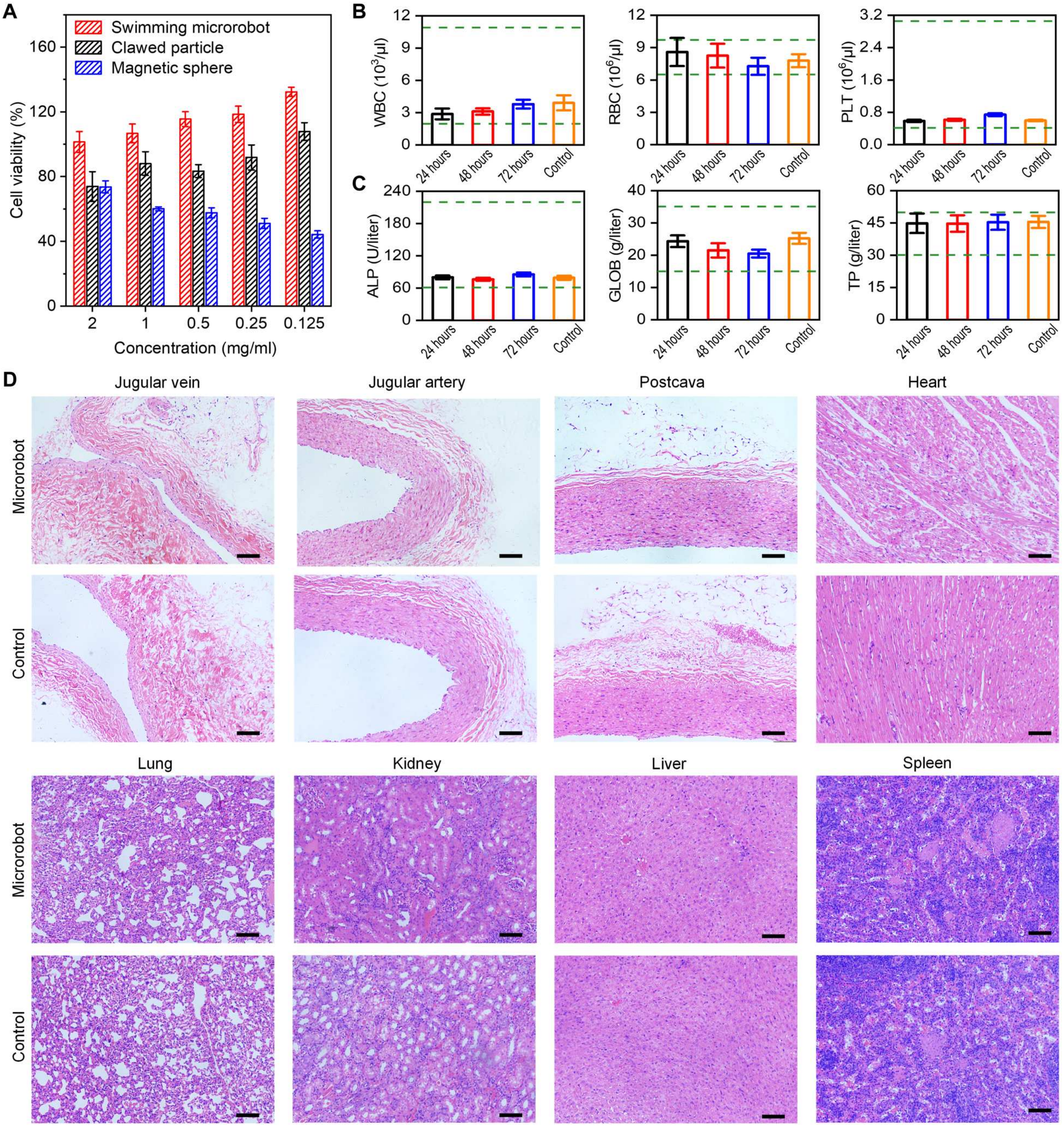

Fig. 6. Biosafety analysis of swimming microrobots. (**A**) Cell viability of human umbilical vein endothelial cell after 24 hours of incubation with swimming microrobots. Comprehensive blood cell counts (**B**) and blood chemistry panel (**C**) taken from nontreated mice and mice with treatment. The green dashed lines indicate the mouse reference ranges of each analyte. WBC, white blood cell; PLT, platelet; ALP, alkaline phosphatase; GLOB, globulin; TP, total protein. (**D**) The major organs were harvested from the swimming microrobot–administrated mice for hematoxylin and eosin (H&E) staining analysis. Scale bars, 200 μm.

microrobots to accomplish their tasks in practice. Third, the prolonged retention of the swimming microrobots, after the application of an external magnetic field in vivo, is of great importance for their use in many practical situations. Although the magnetically actuated movement of swimming microrobots in the blood has been reported in a previous work, they are incapable of withstanding the intensive blood flow experienced, following the removal of the magnetic field.

To address these issues in this work, swimming microrobots were designed with an RBC membrane–camouflaged and magnetically actuated claw engagement, this being inspired by biological features of natural RBCs and the mobility of natural tardigrades on soft plant matter in a dynamic environment. Although the claw engagement design could not offer the swimming microrobots optimal mobility on a rigid substrate, it did allow the movement of the swimming microrobots in the blood vessels, under flow with a rate <2.1 cm/s, which is comparable with that seen in major veins. The magnetically actuated rotation in the *xy* plane allowed the retention of the swimming microrobots for a long period in vessels with a blood FR of up to 3.2 cm/s. Moreover, the use of an RBC membrane–coating on the swimming microrobots reduced the interaction from the blood stream and helped evade the immune system, enabling locomotion and their retention in the blood vessels. The investigations carried out, in both mice and rabbits, confirmed the active, navigated retention of the swimming microrobots in major vein vessels in vivo.

Given that when therapeutic agents are administrated in circulation systems, this mainly relies on passive diffusion in the blood stream, and adherence to the targeted region under intensive blood flow in vivo is particularly challenging for current passive diffusion-based delivery methods. Various targeted delivery designs, including chemical functionalization of therapeutic agents, have been developed, involving molecular interaction with specific groups of target cells, such as are seen in tumors. However, the passive diffusion mechanism, one key part of chemical functionalization strategies, has displayed a limited therapeutic effect, but, by comparison, our platforms facilitate active navigated retention in targeted regions in mice and rabbits through the application of an external magnetic field.

Swimming microrobots can be tailored to support the delivery of various drugs and used in any biological fluid, without additional design being needed. Their navigated locomotion allows the swimming microrobots to arrive in the targeted area. The instantaneous manipulation of the RMF in the *xy* plane has provided the mechanical forces to substantial enhance the adhesion of the swimming microrobots, without the requirement for long-term magnetic actuation in the blood vessels. Such a strategy relies on the capability of the micro/nanostructure used to adsorb polymer gels to act as connectors between polymer chains, which is similar to that seen using nanoparticles in adhesive gels with biological tissues (*52*). Using this strategy, active navigated retention of various cargos, including therapeutic agents and diagnostic particles, is possible without additional and complex design of the microrobots.

The key findings from the investigations carried out support the better conceptual design of swimming microrobots, which couple a controllable propulsion function when magnetically actuated with good mechanical adhesion in the blood vessels, allowing active retention in vivo. The clawed geometry of the swimming microrobots was obtained using thermal processing of pollen to create the clawed template, noting that their thermal treatment removes the main materials of the pollen while maintaining their structure. The materials used for the swimming microrobots, including CHI, ALG, and Fe_3O_4 NPs, are in the category of being "Generally Recognized as Safe" and thus approved for drug delivery. The current fabrication strategy used for the swimming microrobots still faces some issues, particularly in relation to their size and geometry. Further investigations in swimming microrobots with variable geometry and size are expected through the development of advanced fabrication technologies, such as using nanoscribe or glancing angle deposition. Together, the merits of controllable motion and magnetically actuated retention in blood vessels provide considerable promise for the wide use of these swimming microrobots, providing a promising path for drug delivery in other diseases.

MATERIALS AND METHODS

Materials

Sunflower (*Helianthus annuus*) pollen particles were purchased from Greer Laboratories, (Lenoir, NC). Fe(III) isopropoxide, chloroform, methanol, dimethyl silicone oil, and silicon microparticles with diameters of 5 and 20 μm were purchased from Aladdin Chemical Co. Ltd. Square quartz tube was purchased from Sigma-Aldrich. Whole blood and fresh RBCs were collected from male Institute of Cancer Research mice (6 to 8 weeks old; purchased from The First Affiliated Hospital of Harbin Medical University, China), from which the RBC membrane–derived vesicles were derived following a published protocol (*53*). Anti-rabbit CD47 monoclonal antibody (no. 63000) was purchased from Cell Signaling Technology.

Preparation of magnetic clawed particles

The clawed templates were obtained by using sunflower pollens after immersion in a chloroform/methanol (3/1 volume ratio) solution for 24 hours, followed by 1 M hydrochloric acid for 1 hour to remove external pollen kit. The immediate rinsing step before immersing into organic and acid solution was performed for three times and subsequent drying using vacuum aspiration for 5 min at 60°C. Then, the cleaned pollens were coated 50 Fe-O–bearing layers via the layer-by-layer surface sol–gel process according to previous reports (*47*). The pollen particles were first immersed in stirring solution of 0.0125 M Fe(III) isopropoxide in anhydrous 2-propanol for 10 min as one layer. The immediate rinsing steps were carried out for three times using anhydrous 2-propanol to wash residual alkoxide, followed by the washing steps with deionized water for 5 min to hydrolyze the unreacted pendant alkoxide and subsequent vacuum filtration and drying for next layer coating. After coating 50 Fe–O-bearing layers, the pollen particles were attached onto the glass surface and heated in air at a rate of 0.5°C/min to a peak temperature of 600°C. These pollens held at this temperature for 4 hours and dropped to room temperature naturally, generating a magnetic Fe_3O_4 layer on the surface of the microrobot.

Preparation of RBC membrane–derived vesicles

The whole blood withdrawn from male mice was centrifuged at 3000 revolutions per minute (rpm) for 5 min at 4°C and then removed the serum and buffy coat. After washing with ice-cold 1× PBS, the resulting RBCs were suspended in 0.25× PBS in an ice bath for 20 min and were centrifuged at 3000 rpm for 5 min. Intact RBC vesicles were obtained by removing hemoglobin and collecting the pink pellet. The RBC vesicles were subsequently extruded serially through 3000-, 800-, 400-, and 100-nm polycarbonate porous membranes using an Avanti Mini-Extruder (Avanti Polar Lipids).

Swimming microrobots were prepared by five layers of coating of CHI and ALG and one layer of the RBC membranes and were achieved by a layer-by-layer technique (*54*). The magnetic clawed particles were immersed into 2 ml of solution of CHI (1 mg/ml) with positive surface charge for 30 min. After water rinsing to remove the excess CHI, 5 mg of magnetic clawed particles were immersed into 2 ml of negatively charged ALG (1 mg/ml) solution for 30 min. Then, water rinsing was used to remove the extra ALG solution. After that, the magnetic clawed particles were immersed into a suspension of RBC vesicles (size: 50 to 100 nm) for 30 min. Swimming microrobots were obtained after the rinsing step with water, followed by subsequent redispersion in PBS buffer (pH 7.8) at 4°C. Swimming microrobots have high dispersity in aqueous media, with the high negative charge of the RBC membrane preventing aggregation of the particles by electrostatic repulsion. Furthermore, ultraviolet-visible spectroscopy reveals that about 2.5 ng of DOX has been encapsulated in a swimming microrobot.

Characterization of swimming microrobots

SEM images of the swimming microrobots were acquired with a double-beam electron microscopy (Scios2, Thermo Fisher Scientific, USA) at an operating voltage of 10 keV. The samples were coated with a 5-nm carbon layer to improve the conductivity (Leica EM ACE600 Carbon Evaporator). The bright-field and fluorescence microscopic images of swimming microrobots were captured at 25 frame$\cdot$s^{-1} by an inverted optical microscope (Olympus, IX73, Japan) coupled with a Point Grey CCD camera (FLIR, GS3-U3-51S5C/M-C, USA). These video data were analyzed using ImageJ to obtain the trajectories of swimming microrobots. The magnetic hysteresis curve of samples was obtained using a vibrating sample magnetometer (Lake Shore Cryotronics 7404, USA). The viscous force between swimming microrobots and the inner wall of vein was measured by an atomic force microscope (Bruker Instruments, Innova, USA).

Locomotion experiment upon blood flow

The microfluidic chip for model blood flow in vitro was developed using an intravenous infusion tube and a square quartz tube with an outer width of 1.4 mm and inner width of 1.1 mm. The mouse vein was sheathed in the square quartz tube, and its outer wall was pasted on the inner wall of square quartz tube to form a flow channel similar to blood vessel. The flow channel was fixed in a glass, and the glass was fixed inside the magnetic field coils placed on the observation platform of an inverted microscope. In the study of the movement behavior, the swimming microrobots were released in PBS solution or whole blood and introduced into the microfluidic channels using a syringe pump (KD Scientific Inc., Holliston, MA) with controllable FRs. Desired volume FRs (3 to 24 μl/s) were adjusted to generate the required average FRs (0.3 to 2.4 cm/s) inside the square quartz tube.

As for performing upon blood flow in vivo, the mice were given a small amount of heparin sodium intravenously and then operated laparotomy. The venous blood of the mice to was direct introduce into the Y shape flow channel using intravenous infusion tube to establish the upstream motion environment of swimming microrobot. To examine the active navigation on the vein tissues in vivo, swimming microrobots were introduced into one branch of Y shape channel. The blood passing through the flow channel was introduced back into the vein of mice to form a close-loop circle of marine blood flow.

Imaging and control of swimming microrobots in rabbit with an IVOCT system

The Dutch rabbits were anesthetized and then placed in a homemade three-orthogonal Helmholtz coils pair. A high-resolution IVOCT catheter was inserted into its posterior jugular major vein along the direction of blood flow through interventional surgery. The inner cleaning channel of the IVOCT catheter is connected to the imaging area at the end of the catheter, and an external interface is provided to connect with a syringe. The swimming microrobot, mixed in a PBS solution, was drawn into a syringe and injected into the blood vessel through the inner cleaning channel using a syringe pump. The magnetic field with intensity of 30 mT and rotation frequency of 30 Hz was used to carry out magnetic actuation in vivo. The upstream and retention motions of microrobots were continuously imaged by IVOCT scans. At 36 hours after injection of swimming microrobots, the jugular vein was collected and then homogenized in PBS. The amount of DOX was quantified using a Tecan Infinite M200 plate reader based on absorbance readings at 480 nm.

Cell viability tested by CCK-8 assay

Human umbilical vein endothelial cell line HUVEC (ATCC) was first seeded into a 96-well plate at 5×10^4 per well. Once the cells were fully attached, the culture medium was replaced with a fresh medium containing swimming microrobots, clawed particles, and MSs with concentrations of 2, 1, 0.5, 0.25, and 0.125 mg/ml. After 24 hours of incubation, a CCK-8 assay method was used to evaluate the cell viability per the manufacturer′s protocol.

H&E staining analysis of swimming microrobots

To evaluate the safety of swimming microrobots in vivo, we administered 0.05 ml of swimming microrobots suspension Japanese white rabbits weighing 2.5 to 3.0 kg (Experimental Animal Center of the First Affiliated Hospital of Harbin Medical University) through intravascular injection. Healthy rabbits treated with PBS were used as a negative control. Rabbits were euthanized, and various tissues including jugular artery, jugular vein, postcava, lung, kidney, liver, heart, spleen, and stomach, were collected for histological characterization 6 days after administration. To prepare the tissue sample for histology investigation, the tissues were treated with 10% (*v*/*v*) buffered formalin for 15 hours. The longitudinal tissue sections were washed in tissue cassettes and embedded in paraffin. The tissue sections were sliced into 8-mm-thick sections using a freezing microtome (CM1950, Leica) and stained with H&E assay. The samples were imaged with an optical microscope.

All the animals were conducted in accordance with the *Guide for Care and Use of Laboratory Animals*. Animal experiments were permitted by the Experimental Animal Welfare Ethics Committee of Harbin Institute of Technology (no.: IACUC-2021020).

Statistical analysis

All data were shown as means ± SD via at least triplicate samples. A two-tailed, Student′s *t* test was used for testing the significance between two groups. A one-way analysis of variance (ANOVA) with Dunnett′s test was performed to test the significance for multiple comparisons. A statistical significance was assumed at $P < 0.05$. Samples were randomly allocated to different experimental groups. Organisms were cultured and maintained in the same environment and randomly allocated to each group.

Supplementary Materials

This PDF file includes:

Text S1

Figs. S1 to S26

Legends for movies S1 to S7

Other Supplementary Material for this manuscript includes the following:
Movies S1 to S7

REFERENCES AND NOTES

1. J. Li, B. E.-F. de Ávila, W. Gao, L. Zhang, J. Wang, Micro/nanorobots for biomedicine: Delivery, surgery, sensing, and detoxification. *Sci. Robot.* **2**, eaam6431 (2017).
2. T. E. Mallouk, A. Sen, Powering nanorobots. *Sci. Am.* **300**, 72–77 (2009).
3. J. Cui, T.-Y. Huang, Z. Luo, P. Testa, H. Gu, X. Z. Chen, B. J. Nelson, L. J. Heyderman, Nanomagnetic encoding of shape-morphing micromachines. *Nature* **575**, 164–168 (2019).
4. W. Hu, G. Z. Lum, M. Mastrangeli, M. Sitti, Small-scale soft-bodied robot with multimodal locomotion. *Nature* **554**, 81–85 (2018).
5. C. Hu, S. Pane, B. J. Nelson, Soft micro- and nanorobotics. *Annu. Rev. Control. Robot. Auton. Syst.* **1**, 53–75 (2018).
6. X. Wang, C. Ho, Y. Tsatskis, J. Law, Z. Zhang, M. Zhu, C. Dai, F. Wang, M. Tan, S. Hopyan, H. McNeill, Y. Sun, Intracellular manipulation and measurement with multipole magnetic tweezers. *Sci. Robot.* **4**, eaav6180 (2019).
7. P. E. Dupont, B. J. Nelson, M. Goldfarb, B. Hannaford, A. Menciassi, M. K. O'Malley, N. Simaan, P. Valdastri, G. Z. Yang, A decade retrospective of medical robotics research from 2010 to 2020. *Sci. Robot.* **6**, eabi8017 (2021).
8. J. Wang, Will future microbots be task-specific customized machines or multi-purpose "all in one" vehicles? *Nat. Commun.* **12**, 7125 (2021).
9. O. Felfoul, M. Mohammadi, S. Taherkhani, D. de Lanauze, Y. Z. Xu, D. Loghin, S. Essa, S. Jancik, D. Houle, M. Lafleur, L. Gaboury, M. Tabrizian, N. Kaou, M. Atkin, T. Vuong, G. Batist, N. Beauchemin, D. Radzioch, S. Martel, Magneto-aerotactic bacteria deliver drug-containing nanoliposomes to tumour hypoxic regions. *Nat. Nanotechnol.* **11**, 941–947 (2016).
10. M. Medina-Sánchez, O. G. Schmidt, Medical microbots need better imaging and control. *Nature* **545**, 406–408 (2017).
11. A. Gao, R. R. Murphy, W. Chen, G. Dagnino, P. Fischer, M. G. Gutierrez, D. Kundrat, B. J. Nelson, N. Shamsudhin, H. Su, J. Xia, A. Zemmar, D. Zhang, C. Wang, G.-Z. Yang, Progress in robotics for combating infectious diseases. *Sci. Robot.* **6**, eabf1462 (2021).
12. J. Tang, Z. Huo, S. Brittman, H. Gao, P. Yang, Solution-processed core-shell nanowires for efficient photovoltaic cells. *Nat. Nanotechnol.* **6**, 568–572 (2011).
13. S. Sanchez, L. Soler, J. Katuri, Chemically powered micro- and nanomotors. *Angew. Chem. Int. Ed.* **54**, 1414–1444 (2015).
14. F. Meng, A. Ortiz-Ambriz, H. Massana-Cid, A. Vilfan, R. Golestanian, P. Tierno, Field synchronized bidirectional current in confined driven colloids. *Phys. Rev. Res.* **2**, 012025 (2020).
15. H. Zhu, B. Xu, Y. Wang, X. Pan, Z. Qu, Y. Mei, Self-powered locomotion of a hydrogel water strider. *Sci. Robot.* **6**, eabe7925 (2021).
16. B. Dai, J. Wang, Z. Xiong, X. Zhan, W. Dai, C.-C. Li, S.-P. Feng, J. Tang, Programmable artificial phototactic microswimmer. *Nat. Nanotechnol.* **11**, 1087–1092 (2016).
17. D. Blackiston, E. Lederer, S. Kriegman, S. Garnier, J. Bongard, M. Levin, A cellular platform for the development of synthetic living machines. *Sci. Robot.* **6**, eabf1571 (2021).
18. F. Mou, X. Li, Q. Xie, J. Zhang, K. Xiong, L. Xu, J. Guan, Active micromotor systems built from passive particles with biomimetic predator-prey interactions. *ACS Nano* **14**, 406–414 (2020).
19. H. Lu, M. Zhang, Y. Yang, Q. Huang, T. Fukuda, Z. Wang, Y. Shen, A bioinspired multilegged soft millirobot that functions in both dry and wet conditions. *Nat. Commun.* **9**, 3944 (2018).
20. D. Ahmed, T. Baasch, N. Blondel, N. Laubli, J. Dual, B. J. Nelson, Neutrophil-inspired propulsion in a combined acoustic and magnetic field. *Nat. Commun.* **8**, 770 (2017).
21. Y. Dong, L. Wang, V. Iacovacci, X. Wang, L. Zhang, B. J. Nelson, Magnetic helical micro-/nanomachines: Recent progress and perspective. *Matter* **5**, 77–109 (2022).
22. G. Go, S.-G. Jeong, A. Yoo, J. Han, B. Kang, S. Kim, K. T. Nguyen, Z. Jin, C.-S. Kim, Y. R. Seo, J. Y. Kang, J. Y. Na, E. K. Song, Y. Jeong, J. K. Seon, J.-O. Park, E. Choi, Human adipose-derived mesenchymal stem cell-based medical microrobot system for knee cartilage regeneration *in vivo*. *Sci. Robot.* **5**, eaay6626 (2020).
23. B. Wang, K. F. Chan, K. Yuan, Q. Wang, X. Xia, L. Yang, H. Ko, Y.-X. J. Wang, J. J. Y. Sung, P. W. Y. Chiu, L. Zhang, Endoscopy-assisted magnetic navigation of biohybrid soft microrobots with rapid endoluminal delivery and imaging. *Sci. Robot.* **6**, eabd2813 (2021).
24. H. Zhou, C. C. Mayorga-Martinez, S. Pané, L. Zhang, M. Pumera, Magnetically driven micro and nanorobots. *Chem. Rev.* **121**, 4999–5041 (2021).
25. X. Yan, Q. Zhou, M. Vincent, Y. Deng, J. Yu, J. Xu, T. Xu, T. Tang, L. Bian, Y.-X. J. Wang, K. Kostarelos, L. Zhang, Multifunctional biohybrid magnetite microrobots for imaging-guided therapy. *Sci. Robot.* **2**, eaaq1155 (2017).
26. X. Yang, W. Shang, H. Lu, Y. Liu, L. Yang, R. Tan, X. Wu, Y. Shen, An agglutinate magnetic spray transforms inanimate objects into millirobots for biomedical applications. *Sci. Robot.* **5**, eabc8191 (2020).
27. J. Law, X. Wang, M. Luo, L. Xin, X. Du, W. Dou, T. Wang, G. Shan, Y. Wang, P. Song, X. Huang, J. Yu, Y. Sun, Microrobotic swarms for selective embolization. *Sci. Adv.* **8**, eabm5752 (2022).
28. D. Li, C. Liu, Y. Yang, L. Wang, Y. Shen, Micro-rocket robot with all-optic actuating and tracking in blood. *Light Sci. Appl.* **9**, 84 (2020).
29. J. Yu, D. Jin, K.-F. Chan, Q. Wang, K. Yuan, L. Zhang, Active generation and magnetic actuation of microrobotic swarms in bio-fluids. *Nat. Commun.* **10**, 5631 (2019).
30. J. Yu, B. Wang, X. Du, Q. Wang, L. Zhang, Ultra-extensible ribbon-like magnetic microswarm. *Nat. Commun.* **9**, 3260 (2018).
31. P. Fischer, B. J. Nelson, Tiny robots make big advances. *Sci. Robot.* **6**, eabh3168 (2021).
32. Q. Wang, K. F. Chan, K. Schweizer, X. Du, D. Jin, S. C. H. Yu, B. J. Nelson, L. Zhang, Ultrasound doppler-guided real-time navigation of a magnetic microswarm for active endovascular delivery. *Sci. Adv.* **7**, eabe5914 (2021).
33. J. Li, P. Angsantikul, W. Liu, B. E.-F. de Ávila, X. Chang, E. Sandraz, Y. Liang, S. Zhu, Y. Zhang, C. Chen, W. Gao, L. Zhang, J. Wang, Biomimetic platelet-camouflaged nanorobots for binding and isolation of biological threats. *Adv. Mater.* **30**, 1704800 (2018).
34. Z. Wu, Y. Chen, D. Mukasa, O. S. Pak, W. Gao, Medical micro/nanorobots in complex media. *Chem. Soc. Rev.* **49**, 8088–8112 (2020).
35. Y. Alapan, U. Bozuyuk, P. Erkoc, A. C. Karacakol, M. Sitti, Multifunctional surface microrollers for targeted cargo delivery in physiological blood flow. *Sci. Robot.* **5**, eaba5726 (2020).
36. D. Kimono, S. Sarkar, M. Albadrani, R. Seth, D. Bose, A. Mondal, Y. Li, A. N. Kar, M. Nagarkatti, P. Nagarkatti, K. Sullivan, P. Janulewicz, S. Lasley, R. Horner, N. Klimas, S. Chatterjee, Dysbiosis-associated enteric glial cell immune-activation and redox imbalance modulate tight junction protein expression in Gulf War illness pathology. *Front. Physiol.* **10**, 1229 (2019).
37. N. Korin, M. J. Gounis, A. K. Wakhloo, D. E. Ingber, Targeted drug delivery to flow-obstructed blood vessels using mechanically activated nanotherapeutics. *JAMA Neurol.* **72**, 119–122 (2015).
38. T. G. Papaioannou, C. Stefanadis, Vascular wall shear stress: Basic principles and methods. *Hellenic J. Cardiol.* **46**, 9–15 (2015).
39. K. Yuan, B. Jurado-Sánchez, A. Escarpa, Dual-propelled lanbiotic based janus micromotors for selective inactivation of bacterial biofilms. *Angew.Chem. Int. Ed.* **60**, 4915–4924 (2021).
40. F. Peng, Y. Tu, D. A. Wilson, Micro/nanomotors towards *in vivo* application: Cell, tissue and biofluid. *Chem. Soc. Rev.* **46**, 5289–5310 (2017).
41. H. W. Huang, F. E. Uslu, P. Katsamba, E. Lauga, M. S. Sakar, B. J. Nelson, Adaptive locomotion of artificial microswimmers. *Sci. Adv.* **5**, eaau1532 (2019).
42. J. A. Nirody, L. A. Duran, D. Johnston, D. J. Cohen, Tardigrades exhibit robust interlimb coordination across walking speeds and terrains. *Proc. Natl. Acad. Sci. U.S.A.* **118**, e2107289118 (2021).
43. H. T. Lin, B. A. Trimmer, The substrate as a skeleton: Ground reaction forces from a soft-bodied legged animal. *J. Exp. Biol.* **213**, 1133–1142 (2010).
44. C.-M. Hu, R. H. Fang, K.-C. Wang, B. T. Luk, S. Thamphiwatana, D. Dehaini, P. Nguyen, P. Angsantikul, C. H. Wen, A. V. Kroll, C. Carpenter, M. Ramesh, V. Qu, S. H. Patel, J. Zhu, W. Shi, F. M. Hofman, T. C. Chen, W. Gao, K. Zhang, S. Chien, L. Zhang, Nanoparticle biointerfacing by platelet membrane cloaking. *Nature* **526**, 118–121 (2015).
45. C.-M. Hu, R. H. Fang, J. Copp, B. T. Luk, L. Zhang, A biomimetic nanosponge that absorbs pore-forming toxins. *Nat. Nanotechnol.* **8**, 336–340 (2013).
46. W. Lin, M. Kluzek, N. Iuster, E. Shimoni, N. Kampf, R. Goldberg, J. Klein, Cartilage-inspired, lipid-based boundary-lubricated hydrogels. *Science* **370**, 335–338 (2020).
47. W. Brandon Goodwin, I. J. Gomez, Y. Fang, J. C. Meredith, K. H. Sandhage, Conversion of pollen particles into three-dimensional ceramic replicas tailored for multimodal adhesion. *Chem. Mater.* **25**, 4529–4536 (2013).
48. C.-M. J. Hu, L. Zhang, S. Aryal, C. Cheung, R. H. Fang, L. Zhang, Erythrocyte membrane-camouflaged polymeric nanoparticles as a biomimetic delivery platform. *Proc. Natl. Acad. Sci. U.S.A.* **108**, 10980–10985 (2011).
49. C. M. Hu, R. H. Fang, B. T. Luk, L. Zhang, Polymeric nanotherapeutics: Clinical development and advances in stealth functionalization strategies. *Nanoscale* **6**, 65–75 (2014).
50. J. Li, M. Tsubokura, M. Tsunoda, Numerical investigation of the flow around a golf ball at around the critical reynolds number and its comparison with a smooth sphere. *Flow Turbul. Combust.* **95**, 415–436 (2015).
51. N. Korin, M. Kanapathipillai, B. D. Matthews, M. Crescente, A. Brill, T. Mammoto, K. Ghosh, S. Jurek, S. A. Bencherif, D. Bhatta, A. U. Coskun, C. L. Feldman, D. D. Wagner, D. E. Ingber, Shear-activated nanotherapeutics for drug targeting to obstructed blood vessels. *Science* **337**, 738–742 (2012).
52. S. Rose, A. Prevoteau, P. Elziere, D. Hourdet, A. Marcellan, L. Leibler, Nanoparticle solutions as adhesives for gels and biological tissues. *Nature* **505**, 382–385 (2014).

53. J. A. Copp, R. H. Fang, B. T. Luk, C. M. Hu, W. Gao, K. Zhang, L. Zhang, Clearance of pathological antibodies using biomimetic nanoparticles. *Proc. Natl. Acad. Sci. U.S.A.* **111**, 13481–13486 (2014).
54. Z. Wu, J. Li, B. E.-F. de Avila, T. Li, W. Gao, Q. He, L. Zhang, J. Wang, Water-powered cell-mimicking Janus micromotor. *Adv. Funct. Mater.* **25**, 7497–7501 (2015).

Acknowledgments: We thank Z. Cai, W. Sun, Y. Hua, and H. Mu from Shanghai Jiao Tong University for helpful discussions. **Funding:** This work is financially supported by the National Key Research and Development Program (2022YFB4701700), National Natural Science Foundation of China (92048301, 52175009 and 21972035), Heilongjiang Providence Natural Science Foundation of China (YQ2019E018 and YQ2022E022), Natural Science Foundation of Chongqing (CSTB2022NSCQ-MSX0507), Interdisciplinary Research Foundation of HIT (IR20211219 and IR2021112), State Key Laboratory of Robotics (2019-O02), and Fundamental Research Funds for Central Universities. **Author contributions:** J.Z., Z.W., and T.L. conceived the project and supervised the studies. T.L., B.S., and Z.W. carried out the preparation and the characterization of the swimming microrobot. S.Y., Z.Z., and Z.W. characterized the movement of the swimming microrobot. Y.L. and X.W. conducted the IVOCT experiments. Y.P. conducted the AFM experiments. C.S. and Y.R. carried out the fluid simulation analysis. K.T.V.G. edited the manuscript. T.L., S.Y., and Z.W. interpreted the data and cowrote the paper. **Competing interests:** The authors declare that they have no competing interests. **Data and materials availability:** All data needed to evaluate the conclusions in the paper are present in the paper and/or the Supplementary Materials.

Submitted 25 December 2022
Accepted 4 April 2023
Published 5 May 2023
10.1126/sciadv.adg4501

Science Advances

Bioinspired claw-engaged and biolubricated swimming microrobots creating active retention in blood vessels

Tianlong Li, Shimin Yu, Bei Sun, Yilong Li, Xinlong Wang, Yunlu Pan, Chunlei Song, Yukun Ren, Zhanxiang Zhang, Kenneth T.V. Grattan, Zhiguang Wu, and Jie Zhao

Sci. Adv., **9** (18), eadg4501.
DOI: 10.1126/sciadv.adg4501

Science Advances (ISSN) is published by the American Association for the Advancement of Science. 1200 New York Avenue NW, Washington, DC 20005. The title *Science Advances* is a registered trademark of AAAS.